A&A, 701, A230 (2025)
https://doi.org/10.1051/0004-6361/202556081

Astronomy & Astrophysics

The Hot Neptune Initiative (HONEI)

II. TOI-5795 b: A hot super-Neptune orbiting a metal-poor star

F. Manni[1,2,⋆], L. Naponiello[2], L. Mancini[1,2,3], S. Vissapragada[14], K. Biazzo[4], A. S. Bonomo[2], D. Polychroni[2], D. Turrini[2], D. Locci[13], A. Maggio[13], V. D'Orazi[1], M. Damasso[2], C. Briceño[10], D. R. Ciardi[8], C. A. Clark[8], K. A. Collins[5], D. W. Latham[5], N. Law[11], M. López-Morales[16], M. B. Lund[8], L. Malavolta[6,7], A. W. Mann[11], G. Mantovan[6,15], D. Nardiello[6,7], M. Pinamonti[2], D. J. Radford[12], R. P. Schwarz[5], A. Shporer[16], A. Sozzetti[2], C. N. Watkins[5], S. W. Yee[5], C. Ziegler[9], and T. Zingales[6,7]

[1] Department of Physics, University of Rome "Tor Vergata", Via della Ricerca Scientifica 1, 00133 Rome, Italy
[2] INAF – Turin Astrophysical Observatory, via Osservatorio 20, 10025 Pino Torinese, Italy
[3] Max Planck Institute for Astronomy, Königstuhl 17, 69117 Heidelberg, Germany
[4] INAF – Osservatorio Astronomico di Roma, via Frascati 33, 00040 Monte Porzio Catone (RM), Italy
[5] Center for Astrophysics | Harvard & Smithsonian, 60 Garden Street, Cambridge, MA 02138, USA
[6] INAF – Padova Astronomical Observatory, Vicolo dell'Osservatorio 5, Padova 35122, Italy
[7] Department of Physics and Astronomy "Galileo Galilei", University of Padova, Vicolo dell'Osservatorio 3, 35122 Padova, Italy
[8] NASA Exoplanet Science Institute-Caltech/IPAC, Pasadena, CA 91125, USA
[9] Department of Physics, Engineering and Astronomy, S. F. Austin State University, 1936 North St, Nacogdoches, TX 75962, USA
[10] Cerro Tololo Inter-American Observatory, Casilla 603, La Serena, Chile
[11] Department of Physics and Astronomy, The University of North Carolina at Chapel Hill, Chapel Hill, NC 27599-3255, USA
[12] Brierfield Observatory, Bowral, NSW 2576, Australia
[13] INAF – Palermo Astronomical Observatory, Piazza del Parlamento 1, 90134 Palermo, Italy
[14] Carnegie Science Observatories, 813 Santa Barbara Street, Pasadena, CA 91101, USA
[15] Centro di Ateneo di Studi e Attività Spaziali "G. Colombo" – Università degli Studi di Padova, Via Venezia 15, 35131 Padova, Italy
[16] Space Telescope Science Institute, 3700 San Martin Drive, Baltimore, MD 21218, USA

Received 24 June 2025 / Accepted 26 July 2025

ABSTRACT

Context. The formation of Neptune planets with orbital periods shorter than ten days remains uncertain. They might have developed similarly to their longer-period counterparts, emerged from rare collisions between smaller planets, or be the remnant cores of stripped giant planets. Characterising a large number of such planets is important for advancing our understanding of how they form and evolve.
Aims. We aim to confirm the planetary nature and characterise the physical and orbital properties of a close-in Neptune-type transiting exoplanet candidate revealed by TESS around the star TOI-5795 (V = 10.7 mag), 162 pc away from the Sun.
Methods. We monitored TOI-5795 with the HARPS spectrograph for two months to quantify any periodic variations in its radial velocity (RV), necessary to estimate the mass of the smaller companion. We jointly analysed these RV measurements and the TESS photometry. We excluded contaminating sources as the origin of the detected signal using high-angular-resolution speckle and adaptive optical imaging.
Results. We find that the parent star is a metal-poor ([Fe/H] = -0.27 ± 0.07) G3 V star ($T_{\rm eff} = 5718 \pm 50$ K), with a radius of $R_\star = 1.082 \pm 0.026\,R_\odot$, a mass of $M_\star = 0.901^{+0.055}_{-0.037}\,M_\odot$ and an age of $10.2^{+2.5}_{-3.3}$ Gyr. We confirm the planetary nature of the candidate, which can now be named TOI-5795 b. We estimate that the planet has an orbital period of $P_{\rm orb} = 6.1406325 \pm 0.0000054$ days and an orbital eccentricity compatible with zero. With a mass of $23.66^{+4.09}_{-4.60}\,M_\oplus$, a radius of $5.62 \pm 0.11\,R_\oplus$, and an equilibrium temperature of 1136 ± 18 K, it can be considered a hot super-Neptune at the edge of the so-called Neptune desert. The transmission spectroscopy metric of TOI-5795 b is ≈100, which makes it an interesting target for probing the chemical composition of its atmosphere. We simulated planet-formation processes but found almost no successful matches to the observed planet's mass and orbit, suggesting that post-formation dynamical events may have shaped its current state. We also performed an atmospheric-evolution study of TOI-5795 b, finding that this planet likely experienced significant atmospheric stripping due to prolonged high-energy irradiation from its parent star.

Key words. planets and satellites: detection – stars: abundances – stars: fundamental parameters – planetary systems

1. Introduction

The 'Neptune desert' (Mazeh et al. 2016) is a region in the mass-period ($M_{\rm p} - P_{\rm orb}$) space of exoplanets where few Neptune-sized planets ($3\,R_\oplus \lesssim R_{\rm p} \lesssim 7\,R_\oplus$) with short orbital periods and high irradiance have been found, although observational bias should favour the detection of such planets. The dearth of both hot-Neptune and hot-Saturn planets ($10\,M_\oplus \lesssim M_{\rm p} \lesssim 100\,M_\oplus$) might result from the way planets form or migrate. For example, high-eccentricity migration can bring planets very close to their star,

⋆ Corresponding author: francesca.manni@inaf.it

leading to tidal disruption (Matsakos & Königl 2016; Owen & Lai 2018). Additionally, the Neptune desert could be partially explained by the fact that these planets are likely to lose their atmospheres because of intense ultraviolet and X-ray irradiation from their host stars (e.g. Ehrenreich et al. 2015; Ionov et al. 2018; Szabó et al. 2023). Close-in Neptunes can be more susceptible than hot Jupiters to complete evaporation of their envelopes (Owen & Jackson 2012). Photoevaporation can be particularly strong for the puffiest planets because of their proximity to their parent stars and can be further enhanced by Roche-lobe overflow (e.g. Koskinen et al. 2022; Thorngren et al. 2023). Recently, Castro-González et al. (2024a) conducted a study focusing on the Neptunian desert. Based on the Kepler DR25 catalog (Thompson et al. 2018), these authors redefined the boundaries of the desert ($P_{\rm orb} \lesssim 3$ days) and identified a new, highly populated area they term the 'Neptunian ridge', populated by planets with 3.2 days $< P_{\rm orb} <$ 5.7 days, which acts as a transition zone to the 'savanna', a more moderately populated region at greater orbital distances (5.7 to 100 days; see also Bourrier et al. 2018). They also stressed the role of high-eccentricity tidal migration (HEM) and photoevaporation as key processes in shaping this planetary landscape.

Trends have been observed between planet bulk density and stellar metallicity for lightly irradiated ($F_\star < 2 \times 10^8$ erg s^{-1} cm^{-2}) sub-Neptunes (Wilson et al. 2022; Hawthorn et al. 2023; Kunimoto et al. 2023), suggesting that planets orbiting metal-rich stars have metal-rich atmospheres with reduced photoevaporation. However, such a correlation is not evident for lightly irradiated gas giant planets, i.e. 0.1 $M_{\rm Jup} < M_{\rm p} < 4\,M_{\rm Jup}$ (Mantovan et al. 2024b). Although interesting trends are emerging with the sample of Neptunes studied so far, an even larger sample is needed to understand these planets. In this context, we are running the HOt-NEptune Initiative (HONEI; Naponiello et al. 2025b), an observational programme, based on high-resolution spectrographs, with the aim of finding ideal targets for atmospheric follow-up. This is the evolution of a previous GAPS[1] sub-programme (Naponiello et al. 2022, 2023, 2025a) and is specifically designed to confirm and characterise hot- and warm Neptune-sized TESS objects of interest (TOIs) in different environments with the aim of investigating their origin.

Here, we report the results of multi-instrument observations of the star TOI-5795, which allowed us to measure the mass of the planet candidate TOI 5795.01, confirming its planetary nature and characterising its main physical and orbital parameters.

This paper is structured as follows. Sect. 2 describes the photometric, spectroscopic, and high-angular-resolution-imaging observations on which this work is based. Section 3 details the physical and atmospheric parameters of the parent star. The analysis of the planetary signal and the subsequent characterisation of the planetary system, by a joint analysis of different data sets, are described in Sect. 4. The possible formation and evolution scenarios of TOI-5795 b are analysed in Sect. 5, while the evolutionary history of its atmosphere is investigated in Sect. 6. Our conclusions are summarised in Sect. 7.

2. Observations and data reduction

2.1. TESS photometry

The target of this study is the star TIC 151724385 (also known as 2MASS J20192849-0732511; $Tmag$ = 10.19 mag; see Table 1), which is located ≈160 pc away and was observed by TESS, as a preselected target (Stassun et al. 2019), from July 9 to August 5,

[1] Global Architecture of Planetary Systems (e.g. Esposito et al. 2014).

Table 1. Astrometric, spectroscopic, and photometric parameters for TOI-5795.

Parameter	Unit	Value	Source
Cross-identifications			
TOI ID		5795	TOI cat.
TIC ID		151724385	TIC
TYC ID		5741-424-1	TYC
GSC ID		05741-00424	GSC
2MASS ID		J20192849-0732511	2MASS
Gaia DR1 ID		4216036345540368768	Gaia DR1
Gaia DR3 ID		4216036349838071424	Gaia DR3
Astrometric properties			
α (J2000)	h:m:s	20 : 19 : 28.51	Gaia DR3
δ (J2010)	d:m:s	−07 : 32 : 51.57	Gaia DR3
π	mas	6.1900 ± 0.0213	Gaia DR3
μ_α	mas yr^{-1}	12.8097 ± 0.0233	Gaia DR3
$\cos_\delta$	mas yr^{-1}	−29.7160 ± 0.0152	Gaia DR3
Photometric properties			
B_T	mag	11.466 ± 0.135	Tycho-2
V_T	mag	10.708 ± 0.009	Tycho-2
g'	mag	11.107 ± 0.026	APASS Sloan
r'	mag	10.629 ± 0.026	APASS Sloan
i'	mag	10.512 ± 0.073	APASS Sloan
$TESS$	mag	10.187 ± 0.006	TIC v8.2
G	mag	10.6376 ± 0.000361	Gaia DR3
BP	mag	10.9813 ± 0.0007	Gaia DR3
RP	mag	10.1264 ± 0.0003	Gaia DR3
J	mag	9.557 ± 0.021	2MASS
H	mag	9.218 ± 0.021	2MASS
K	mag	9.168 ± 0.021	2MASS
$W1$ 3.4 µm	mag	9.114 ± 0.022	AllWISE
$W2$ 4.6 µm	mag	9.146 ± 0.020	AllWISE
$W3$ 12 µm	mag	9.109 ± 0.033	AllWISE
Spectroscopic properties			
Spectral type		G3 V	This work[(a)]
$v \sin i$	km s^{-1}	1.9 ±1.0	This work
[Fe/H]	dex	−0.27 ± 0.07	This work
[C/H]	dex	−0.27 ± 0.05	This work
[S/H]	dex	−0.21 ± 0.07	This work
[O/H]	dex	−0.20 ± 0.10	This work
[Mg/H]	dex	−0.06 ± 0.08	This work
[Si/H]	dex	−0.14 ± 0.08	This work
Derived parameters			
$L_\star$	$L_\odot$	1.130 ± 0.043	This work
$M_\star$	$M_\odot$	$0.901^{+0.055}_{-0.037}$	This work
$R_\star$	$R_\odot$	1.082 ± 0.026	This work
$\log g_\star$	cgs	4.32 ± 0.13	This work
$\rho_\star$	g cm^{-3}	$1.008^{+0.091}_{-0.073}$	This work
$\log R'_{\rm HK}$	dex	−5.07 ± 0.02	This work[(b)]
$T_{\rm eff}$	K	5715 ± 55	This work
Age	Gyr	$10.2^{+2.5}_{-3.3}$	This work
A_V	mag	<0.094	This work
Distance	pc	161.5 ± 0.6	This work
$\gamma_{\rm RV}$	m s^{-1}	−66962.3	This work

Notes. [(a)]The spectral type has been derived from the tables of Pecaut & Mamajek (2013) (version 2022) and using our $T_{\rm eff}$ value. [(b)]The $\log R'_{\rm HK}$ has been derived using the `ACTIN2` code (`https://github.com/gomesdasilva/ACTIN2`) v2.0 beta11 (Gomes da Silva et al. 2018) from the combined HARPS spectra. **References:** TESS Primary Mission TOI catalog (Guerrero et al. 2021); TIC (Stassun et al. 2018, 2019); Tycho (Høg et al. 2000); APASS Johnson (Henden et al. 2016); 2MASS (Skrutskie et al. 2006); *Gaia* DR3 (Gaia Collaboration 2023); AllWISE (Cutri et al. 2021).

2022, during Sector 54 of its first extended mission. It became a TOI on September 22, 2022 and was catalogued as TOI-5795. It was observed again by TESS from July 15 to August 10, 2024, during Sector 81 of its second extended mission, and then from May 7 to June 3, 2025, during Sector 92. In all sectors, the target was observed with a 2-min cadence and a total of 30 086 images were collected. The three TESS light curves span about 763 days and contain 12 transit events[2] of the planet candidate TOI 5795.01 with an average depth of 2.86 ± 0.16 mmag (see Fig. 1).

We downloaded the TESS light curves of TOI-5795 as a `LightCurveFile` object, from the Mikulski Archive for Space Telescopes (MAST) using the Python package `lightkurve` (Lightkurve Collaboration 2018). The `LightCurveFile` object contains both the Simple Aperture Photometry (SAP; Twicken et al. 2010) and the Presearch Data Conditioning SAP flux (PDC-SAP; Smith et al. 2012; Stumpe et al. 2012, 2014), which were extracted with the TESS Science Processing Operation Centre (SPOC) pipeline (Jenkins et al. 2016). Potential contaminating sources within the TESS aperture, which could lead to a shallower transit depth than the actual value, are typically addressed using a dilution factor. Here, the PDC-SAP photometry was corrected for contamination from other objects using the Create Optimal Apertures module (Bryson et al. 2010, 2020). However, in this case, there are no sources close to the borders of the SPOC pipeline aperture, as shown in Fig. A.1, where the apertures were drawn using `tpfplotter` [3] (Aller et al. 2020) for Sectors 54, 81, and 92 together with the closest sources extracted from the *Gaia* satellite DR3 catalogue.

2.2. Ground-based photometric follow-up observations

Ground-based follow-up observations in search of transits of TOI-5795 b were carried out by members of the TESS Follow-up Observing Program Working Group and are archived at ExoFOP.

A complete transit of TOI-5795 b was observed on 25 June, 2023 through a Pan-STARRS z_s filter (wavelength centre 8700 Å) using the $f/8$ Ritchey-Chretien 1-m telescope, from the Las Cumbres Observatory Global Telescope (LCOGT) (Brown et al. 2013) at the Cerro Tololo Inter-American Observatory in Chile (CTIO). This telescope is equipped with the SINISTRO camera with 4096 × 4096 pixels and a pixel size of 15 µm. The resulting plate scale is 0.389 arcsec pixel^{-1}, which gives a 26′ × 26′ field of view. The images were calibrated using the standard LCOGT `BANZAI` pipeline (McCully et al. 2018), and differential photometric data were extracted using `AstroImageJ` (Collins et al. 2017). A circular 5.″8 photometric aperture was adopted to exclude all flux from the nearest known neighbour in the *Gaia* DR3 catalogue (Gaia DR3 4216036345540514432), which lies 17.″8 to the north-east of TOI-5795.

Another complete transit was observed on September 15, 2024 through a Johnson/Cousins B band filter using the 0.36 m $f/7.2$ Corrected Dall-Kirkham Astrograph telescope at the Brierfield Observatory near Bowral, New South Wales, Australia. This telescope is equipped with a Moravian G4-16000 KAF-16803 camera, which has 4096 × 4096 pixels and a pixel size of 9 µm. The plate scale is 1.47 arcsec pixel^{-1}, resulting in a 50′ × 50′ field of view. The differential photometric data were also extracted using `AstroImageJ` by adopting a circular 5.″9 photometric aperture. The final LCO and Brierfield light curves from the global fit are shown in Fig. 7, together with the phase-folded PDC-SAP light curve.

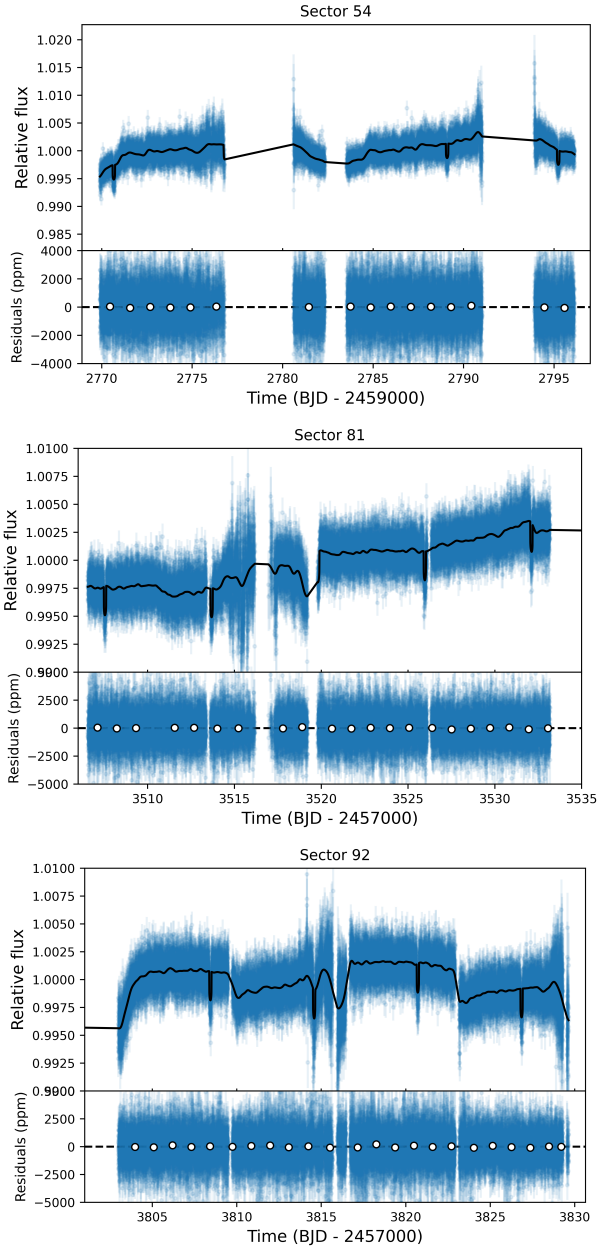

Fig. 1. Light curve of TOI-5795 obtained by TESS by monitoring Sectors 54 (top panel), 81 (middle panel), and 92 (bottom panel) at a 2-min cadence, extracted using the SAP pipeline. No significant rotational modulation is detected. The black line represents our best-fit transit model, while the white points are binned data. The residuals of the best-fit model are shown in parts per million in all panels.

2.3. High-angular-resolution imaging

High-angular-resolution imaging is essential to identify nearby sources that can contaminate the TESS photometry, resulting in an underestimated planetary radius, or to identify sources of

[2] A comment in the ExoFOP-TESS database (Akeson et al. 2013) refers to a possible additional transit event at ~2757 (BJD − 2 457 000); however, this timestamp is prior to the start of the available light curves, making such an event impossible. It likely refers instead to a dip at ~2787. This feature is probably due to an off-target eclipsing binary blend, particularly since the first flagged event near ~2772 is shallower, exhibits some depth–aperture correlation, and is likely a secondary eclipse.

[3] https://github.com/jlillo/tpfplotter/

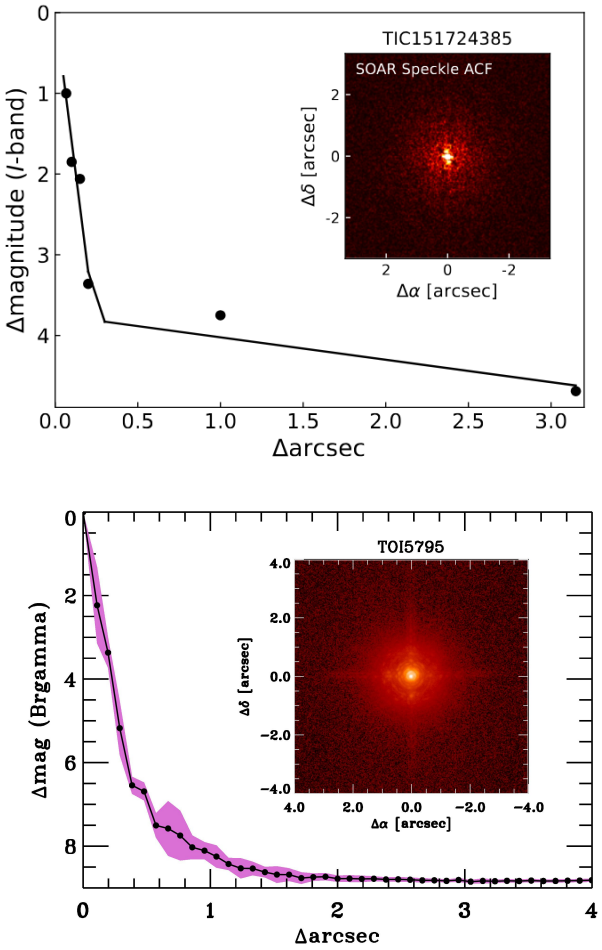

Fig. 2. High-resolution sensitivity curves for SOAR (top panel) and the Palomar Hale telescope (bottom panel), plotted as a function of angular separation from the host star. Insets in the respective panels show images of the central region of the data.

astrophysical false positives, such as background eclipsing binaries (Ciardi et al. 2015). As part of our standard process for validating transiting exoplanets, TOI-5795 was observed using optical speckle and near-infrared adaptive-optical (AO) imaging.

2.3.1. Optical speckle imaging

We searched for stellar companions to TOI-5795 using speckle imaging on the 4.1-m Southern Astrophysical Research (SOAR) telescope (Tokovinin et al. 2018) on November 4, 2022, observing in the Cousins-*I* band, a bandpass similar to that of TESS. This observation was sensitive to $5\,\sigma$ detections of stars 3.9 magnitudes fainter at an angular distance of 1″ from the target. Further details of the observations within the SOAR TESS survey are available in Ziegler et al. (2020). The $5\,\sigma$ detection sensitivity and speckle autocorrelation functions for TOI-5795 observations are shown in the top panel of Fig. 2. No nearby stars were detected within 3″of TOI-5795 in the SOAR observations.

2.3.2. Near-infrared AO imaging

Observations of TOI-5795 were made on August 29, 2023, with the Palomar High Angular Resolution Observer (PHARO) instrument (Hayward et al. 2001) on the Palomar Hale 5.1-m telescope, behind the P3K natural guide star AO system (Dekany et al. 2013). The pixel scale for PHARO is 0.025″. Palomar data were collected in a standard five-point quincunx dither pattern in the Br-γ filter (λ_0 = 2166 µm; $\Delta\lambda$ = 0.020 µm). The reduced science frames were combined into a single mosaic image with a final resolutions of ∼0.095″.

The sensitivity of the final combined AO images was determined by injecting simulated sources azimuthally around the primary target every 20°, at separations of integer multiples of the central source full width at half maximum (FWHM) (Furlan et al. 2017). The brightness of each injected source was scaled until standard aperture photometry detected it with $5\,\sigma$ significance. The final $5\,\sigma$ limit at each separation was determined from the average of all limits at that separation, and the uncertainty in each limit was established by the rms dispersion of the azimuthal slices at a given radial distance. No stellar companions were detected, with the images reaching a contrast of ∼3.9 (SOAR) and ∼7.5 (Palomar) magnitudes fainter than TOI-5795 within 0.5″ in each respective band (see Fig. 2).

2.4. Spectroscopic observations

Spectroscopic follow-up observations and radial-velocity (RV) measurements of TOI-5795 were obtained with TRES (Tillinghast Reflector Échelle Spectrograph; Szentgyorgyi & Furész 2007) and HARPS (High Accuracy Radial velocity Planet Searcher; Pepe et al. 2002; Mayor et al. 2003).

The Tillinghast Reflector Echelle Spectrograph (TRES) is a fibre echelle spectrograph (R = 44 000) mounted on the 1.5-metre Tillinghast telescope at the Smithsonian Astrophysical Observatory's Fred L. Whipple Observatory on Mount Hopkins in Arizona, USA. Two reconnaissance spectra of TOI-5795 were obtained in October 2022, revealing a G-dwarf. No significant RV variations were found in the two initial spectra, ruling out binary scenarios. Additional spectra of this star were collected to search for possible long-term RV trends. In total, 13 TRES observations were recorded over a 2-year span. The derived RVs have an average precision of 27.7 m s^{-1} (see Table A.1), consistent with no detectable RV variation due to the TESS planet candidate, or to external long-period objects orbiting around TOI-5795. Details regarding the detection sensitivity of this dataset are provided in Appendix B, together with those of HARPS.

2.4.1. HARPS data

HARPS is a high-resolution (R = 115 000), visible-light, fibre-fed echelle spectrograph mounted on the ESO 3.6-meter telescope at La Silla, Chile. Due to its long-term stability and simultaneous wavelength calibration, HARPS is one of the few instruments currently in operation that can achieve, under optimal conditions, RV measurements with an accuracy of ∼1 m s^{-1} (Pepe et al. 2014). We monitored TOI-5795 in summer 2024, from June 29 to August 13, under ESO programme 113.26UJ (PI: Naponiello), collecting a total of 19 RV measurements with an average S/N of 27 (see Table A.1). We used the fibre-AB spectroscopy mode (object and sky) with an exposure time of 20 min. The spectra were calibrated and the RVs derived using the SpEctrum Radial Velocity Analyzer (SERVAL) pipeline (Zechmeister et al. 2018), resulting in an average RV uncertainty of 2.7 m s^{-1}.

We also investigated various stellar activity indicators in this dataset, including the bisector inverse slope (BIS), the FWHM,

the line contrast of the cross-correlation function (CCF), and the chromospheric activity index $\log R'_{\rm HK}$, as well as the cores of the sodium (Na I), helium (He I), and Hα spectral lines (extracted with `ACTIN2`; Gomes da Silva et al. 2018). None of these indicators showed significant periodic signals, with all generalised Lomb-Scargle (GLS) periodograms returning false alarm probabilities (FAP) above 15%.

3. Host-star characterisation

To estimate the photospheric parameters of the host star, we produced a co-added spectrum from the HARPS spectra (see Sect. 2.4.1). The S/N of the co-added spectrum was ∼160 at λ∼6000 Å. From this spectrum, we derived the spectroscopic atmospheric parameters, i.e. the effective temperature ($T_{\rm eff}$), surface gravity ($\log g$), microturbulence velocity (ξ), and iron abundance ([Fe/H]), using equivalent widths (EWs) of iron lines (see Biazzo et al. 2022 for details). EWs were measured using the ARESv2 code (Sousa et al. 2015). We then adopted the Castelli & Kurucz (2003) grid of model atmospheres with new opacities (ODFNEW) and the spectral package pymoogi (Adamow 2017), which is a wrapper of the MOOG code (version 2019; Sneden 1973). We also computed the elemental abundances of magnesium, silicon, carbon, and sulphur using the procedure based on line EWs and the same codes and grid of models as above. Finally, following the spectral synthesis method described by Biazzo et al. (2022) and assuming the macroturbulence velocity $v_{\rm macro}$ = 3.3 km s^{-1} by Doyle et al. (2014), we find a projected rotational velocity $v \sin i$ = 1.9 ± 1.0 km s^{-1}, which is at the limit of the HARPS spectral resolution. The same procedure was applied to the TRES spectrum with the highest S/N to derive the oxygen abundance from the infrared triplet lines (at ∼7772 − 7775 Å) and applied the non-LTE (NLTE) corrections by Amarsi et al. (2015). All stellar parameters and elemental abundances are listed in Table 1. It is worth noting that the star is metal-poor, i.e. [Fe/H] = −0.27 ± 0.07.

We determined the stellar mass, radius, and age using the `EXOFASTv2` differential evolution Markov chain Monte Carlo tool (Eastman 2017; Eastman et al. 2019), by simultaneously modelling the stellar spectral energy distribution (SED) and the MESA Isochrones and Stellar Tracks (MIST; Paxton et al. 2015); see Naponiello et al. (2025a) for more details. We sampled the SED with the Tycho-2 $B_{\rm T}$ and $V_{\rm T}$, APASS Johnson B, V, g', r', and i', 2MASS J, H, and $K_{\rm s}$, and WISE $W1$, $W2$, and $W3$ magnitudes (see Table 1 and Fig. 3). We imposed Gaussian priors on the *Gaia* DR3 parallax, as well as on the $T_{\rm eff}$ and [Fe/H], as derived from our spectral analysis. The fitted and derived parameters of the host star are given in Table 1. The estimated old age of ∼10 Gyr is consistent with both the low $\log R'_{HK}$ = −5.07 ± 0.02 and the absence of significant variations due to stellar activity in the light curve and in the activity-spectrum indices.

4. Physical and orbital characterisation of the TOI-5795 planetary system

4.1. Periodogram of the RV time series

In the RVs obtained with HARPS, we searched for the same periodic signal present in the TESS light curve using the GLS periodogram (Zechmeister & Kürster 2009), using the Python package `astropy` v.5.2.2 (Astropy Collaboration 2018). The orbital period of the planet candidate TOI 5795.01 is clearly identified as the highest peak in the periodogram (see Fig. 4).

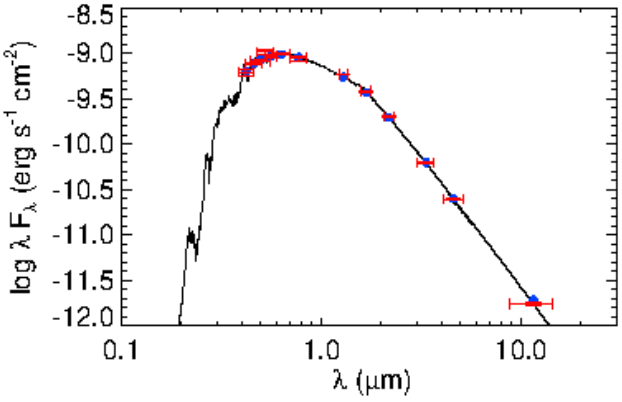

Fig. 3. Stellar spectral energy distribution (SEDs). The broadband measurements from the Tycho, APASS Johnson and Sloan, 2MASS, and WISE surveys are shown in red, and the corresponding theoretical values are shown as blue circles. The non-averaged best-fit model is plotted as a black solid line.

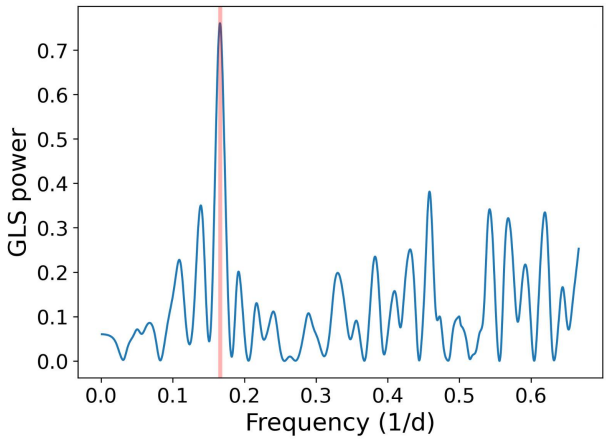

Fig. 4. Generalised Lomb-Scargle (GLS) periodogram of HARPS RV measurements of TOI-5795, showing the main peak correctly identified at ∼6 days.

Often, no additional signals appear in the first RV periodogram because the principal signal is too strong; however, once this is removed, secondary signals emerge in the residual periodogram. While, the residuals of the one-planet model exhibit some scatter, the limited number of RV data points makes it difficult to confidently identify any additional signals that might be present, and no significant signals are revealed in the GLS periodogram of the residuals of the one-planet model. Furthermore, no other transit signals are detected in the light curve.

4.2. Global modelling of the data

We performed a joint modelling of the TESS photometry, ground-based follow-up photometry, and HARPS-RV data following our consolidated procedure, as described in Naponiello et al. (2022, 2023, 2025a). Briefly, we used the Python wrapper `juliet`[4] (Espinoza et al. 2019), which utilises `batman`[5]

[4] https://juliet.readthedocs.io/
[5] https://github.com/lkreidberg/batman

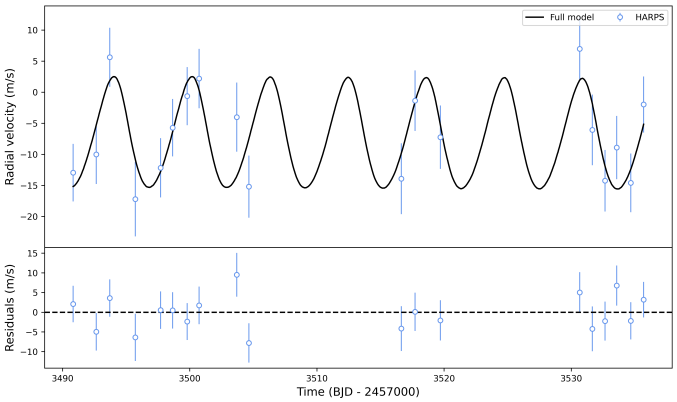

Fig. 5. Top panel: HARPS RV measurements of TOI-5795 in blue, with the preferred model fit shown in black. Bottom panel: RV residuals over the model fit.

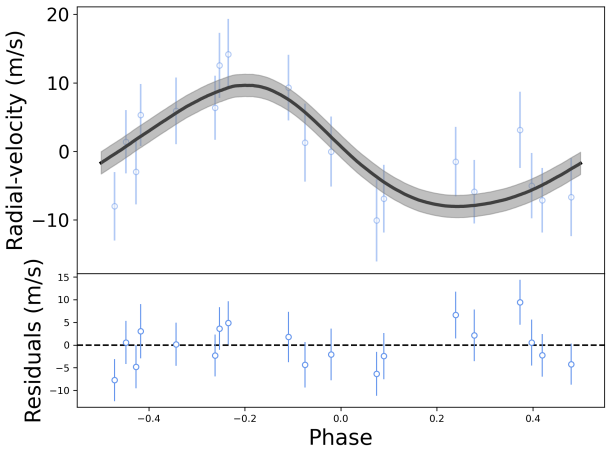

Fig. 6. Top panel: phase-folded HARPS RV measurements of TOI-5795 in blue, with the preferred model fit in black. Bottom panel: RV residuals over the model fit. The error bars include both the data uncertainty and the jitter derived from the analysis.

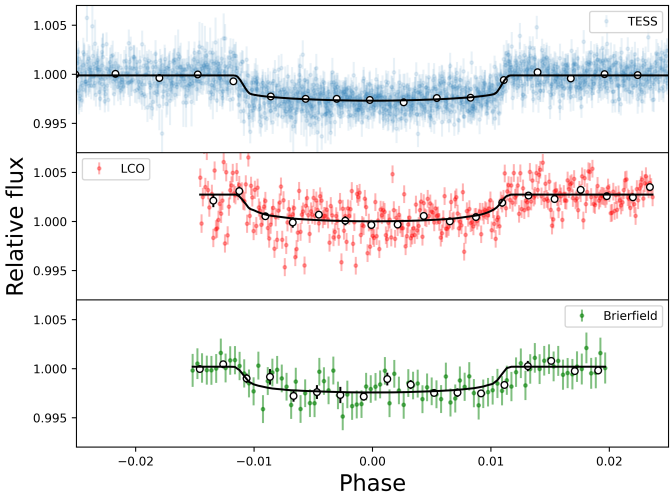

Fig. 7. Global fit result for TESS and ground-based observations. The superimposed points correspond to phase-bins of 22 minutes, 18 minutes, and 17 minutes for TESS, LCO and Brierfield, respectively. The error bars include both the data uncertainty and the jitter from the analysis.

(Kreidberg 2015) and `RadVel`[6] (Fulton et al. 2018), for the modelling of transit and RV data, respectively. The systematics (red noise) in the photometric time series were modelled by means of Gaussian processes (GPs) via the `celerite` package (Foreman-Mackey et al. 2017). A Bayesian approach, based on the dynamic nested sampling package `dynesty` (Speagle 2020), was then adopted to explore the posterior distribution of the model parameters and estimate the Bayesian evidence, ensuring consistency with the data.

The joint RV and photometry analysis was run for a simple one-planet model. For the RV dataset, only for uncorrelated (white) noise was taken into account. Large uniform (uninformative) priors were used for the distribution of all parameters. In particular, the priors for $P_{\rm orb}$ and T_0 were centred around the values reported in the data validation report produced by the TESS SPOC (Jenkins et al. 2016) pipeline. The best-fitting values and uncertainties for the transit, RV, and Keplerian parameters were then derived from the posterior probability distributions. Following Eastman et al. (2013), the eccentricity, e, and the argument of periastron, ω, were parametrised as $\sqrt{e}\sin\omega$ and $\sqrt{e}\cos\omega$. The impact parameter, b, and the ratio of the radii of the star and the planet, $k = R_{\rm p}/R_\star$, were parametrised as r_1 and r_2 (see Espinoza 2018). For the limb-darkening (LD) coefficients, we adopted the same parameterisation as Kipping (2013), i.e. $q_1 \equiv (u_1 + u_2)^2$ and $q_2 \equiv 0.5\,(u_1 + u_2)^{-1}$, where u_1 and u_2 are the LD coefficients of the quadratic law.

HARPS RVs are shown in Figs. 5 and 6 (phase-folded), together with the preferred global model (top panels) and its residuals (bottom panels). The TESS, LCO, and Brierfield light curves of TOI-5795, folded with the planet's orbital period, are plotted in Fig. 7 together with the best-fit transit models resulting from the global fit. The posterior estimates of the main parameters of the joint fit are reported in Table 2. We therefore confirm the planetary nature of the TESS candidate TOI 5795.01, hereafter referred to as TOI-5795 b, with a mass of $M_{\rm p} = 23.66^{+4.09}_{-4.60}\,M_\oplus$ (e.g. $> 5\sigma$ significance), a radius of $R_{\rm p} = 5.62 \pm 0.11\,R_\oplus$, corresponding to a bulk density of $0.73 \pm 0.13\,{\rm g\,cm^{-3}}$ (compatible with that of Saturn, $0.69\,{\rm g\,cm^{-3}}$) and an equilibrium temperature of $T_{\rm eq} = 1136 \pm 18$ K. Consequently, it can be considered as a hot super-Neptune and its orbital period (6.14 days) places it at the edge of the Neptune ridge (according to the framework by Castro-González et al. 2024a), i.e. at the beginning of the so-called 'savanna' (see Fig. 8 and the discussion in Sect. 7). The orbital eccentricity of TOI-5795 b was estimated as $e = 0.15 \pm 0.06$ and is therefore compatible with zero at 95.5% confidence, although the Bayesian evidence is slightly in favour of the circular scenario ($\Delta \ln \mathcal{Z}^{e=0}_{e\geq 0} < 3$). Finally, we note that the measured RV jitter is higher than expected ($3.75^{+1.23}_{-1.08}$; see Table 2), particularly given the relatively quiet nature of TOI-5795. This may be attributed to unresolved signals not captured within our limited temporal baseline. Continued RV monitoring is recommended to better characterise any additional variability.

5. The formation and evolution of TOI-5795 b

We used the Monte Carlo version of the `GroMiT` (planetary GROwth and MIgration Tracks) code (Polychroni et al. 2023) to investigate the possible formation history of TOI-5795 b, following Mantovan et al. (2024b) and Naponiello et al. (2025a). The simulations were based on the pebble accretion model, adopting

[6] https://radvel.readthedocs.io

Table 2. Orbital and physical parameters of TOI-5795 b.

Parameter	Unit	Value
Light curve parameters		
$P_{\rm orb}$	day	6.1406325 ± 0.0000054
T_0	$\rm BJD_{TDB}$	$2\,459\,770.67397^{+0.00060}_{-0.00061}$
T_{14}	hr	$3.407^{+0.028}_{-0.026}$
$R_{\rm p}/R_\star$		0.0477 ± 0.0006
b		$0.29^{+0.12}_{-0.14}$
i	deg	$88.54^{+0.68}_{-0.55}$
$a/R_\star$		$12.65^{+0.34}_{-0.35}$
Limb-darkening coefficients[(a)]		
q_1, TESS		$0.20^{+0.15}_{-0.08}$
q_2, TESS		$0.41^{+0.33}_{-0.24}$
q_1, B		$0.42^{+0.36}_{-0.29}$
q_2, B		$0.52^{+0.31}_{-0.29}$
q_1, LCO		$0.50^{+0.33}_{-0.32}$
q_2, LCO		$0.54^{+0.32}_{-0.33}$
RV parameters		
K	$\rm m\,s^{-1}$	$8.97^{+1.51}_{-1.74}$
$\sqrt{e}\sin\omega$		$0.197^{+0.101}_{-0.105}$
$\sqrt{e}\cos\omega$		$0.317^{+0.107}_{-0.142}$
e[(b)]		< 0.25
ω	deg	$31.67^{+25.07}_{-17.83}$
RV jitter HARPS	$\rm m\,s^{-1}$	$3.75^{+1.23}_{-1.08}$
Derived		
$M_{\rm p}$	$M_\oplus$	$23.66^{+4.09}_{-4.61}$
$R_{\rm p}$	$R_\oplus$	5.62 ± 0.11
$\rho_{\rm p}$	$\rm g\,cm^{-3}$	0.73 ± 0.13
$\log g_p$	cgs	7.33 ± 1.29
a	au	0.064 ± 0.002
$T_{\rm eq}$[(c)]	K	$1136.78^{+18.89}_{-18.02}$
TSM[(d)]		103^{+25}_{-15}
GP coefficients		
$\sigma_{\rm GP}$		0.00160 ± 0.00014
$\rho_{\rm GP}$		0.98 ± 0.09

Notes. The median values of the best-fit parameters for TOI-5795 b, along with their upper and lower 68% credibility intervals as uncertainties. These values, both fitted and derived, were obtained from the posterior distributions of the corresponding models. [(a)] $q_1 \equiv (u_1 + u_2)^2$ and $q_2 \equiv 0.5\,(u_1 + u_2)^{-1}$, where u_1 and u_2 are the LD coefficients of the quadratic law (Kipping 2013). [(b)] The 95% ($2\,\sigma$) confidence upper limit on the eccentricity determined when $\sqrt{e}\cos\omega$ and $\sqrt{e}\sin\omega$ are allowed to vary in the fit. [(c)] This represents the equilibrium temperature assuming a Bond albedo of zero and an uniform redistribution of heat to the night side. [(d)] Transmission spectroscopy metric (TSM; Kempton et al. 2018).

the treatment for the growth and migration of solid- and gas-accreting planets from Johansen et al. (2019) and Tanaka et al. (2020), respectively. We used the scaling law for the pebble isolation mass from Bitsch et al. (2018) to explore the formation of 10^5 planetary seeds embedded in a plausible native protoplanetary disc with mass equal to 5% that of the star and characteristic

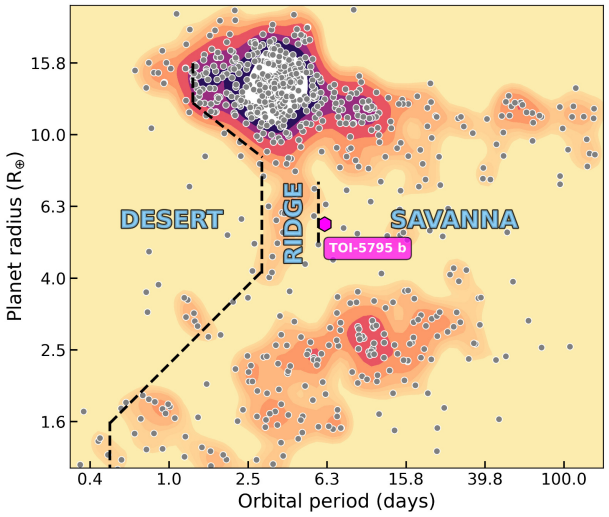

Fig. 8. Radius-period diagram of close-in exoplanets with mass and radius measured to an accuracy of at least $5\,\sigma$. The data were obtained from the NASA Exoplanet Archive on February 13, 2025. Error bars have been suppressed for clarity. The position of TOI-5795 b is highlighted, together with the population-based boundaries of the Neptunian desert, ridge, and savanna, as derived by Castro-González et al. (2024a). This plot was generated with `nep-des` (`https://github.com/castro-gzlz/nep-des`).

radius of 60 au (i.e. following the solar nebula-like template from Turrini et al. 2023). The protoplanetary disc is described by a steady state viscous disc (Johansen et al. 2019; Armitage 2020) characterised by mass loss due to photoevaporation of 10^{-9} $\rm M_\odot\ yr^{-1}$ (Tanaka et al. 2020) and a thermal profile due to viscous heating and stellar irradiation, following the prescription of Ida et al. (2016). The pebble-to-gas ratio in the different regions of the disc was computed from the stellar metallicity, given in Table 1, using the condensation profile from Turrini et al. (2023). We used the stellar evolutionary models of Baraffe et al. (2015) to set the pre-main sequence luminosity to $1.23\,L_\odot$, as predicted for a star with a mass similar to that of TOI-5795 at 1.5 Myr.

The simulations followed the planet formation process for 5 Myr. Planetary seeds were randomly placed on the disc, varying (i) their initial semi-major axis (0.1–60 au), (ii) their input time (0.1 yr − 3 Myr), and (iii) the disc viscosity coefficient within the range reported in Rosotti (2023). We considered both mm- and cm-sized pebble-dominated discs. The success rate in producing synthetic planets within $3\,\sigma$ of the observed semi-major axis and the mass of the real planet proved extremely limited. This prompted us to run further sets of simulations. We first explored the impact of more efficient pebble accretion using pebble sizes from 1 cm to 1 dm, for a total of 3×10^5 additional simulations. In Fig. 9, we plot the cumulative results of all these simulations, overplotting the current semi-major axis and mass of the planet. Once again, reproducing TOI-5795 b proved difficult in the framework of pebble accretion, as we found only one object within $3\,\sigma$ of the planet, out of a total of 4×10^5 synthetic planets.

We then explored whether this lack of matching outcomes could be due to the chosen disc conditions, as pebble accretion strongly depends on the properties of the environment in which it takes place. We ran further simulation campaigns, changing the initial mass and characteristic radius of the circumstellar disc based on the results of observational surveys from Testi et al. (2022) and Andrews (2020). Specifically, we considered disc

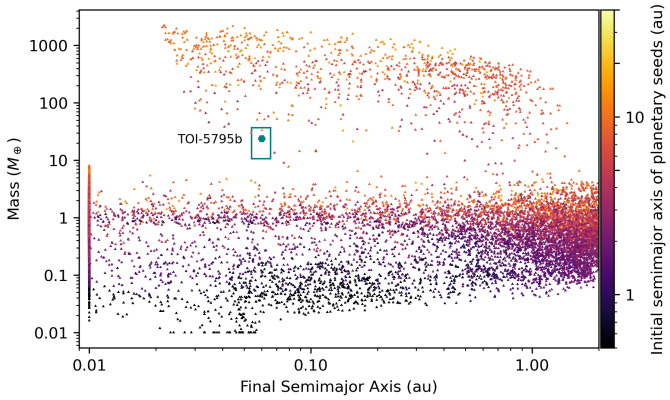

Fig. 9. Synthetic population of 4×10^5 exoplanets formed in a plausible native protoplanetary disc of TOI-5795 b. The synthetic planets are plotted in the final semi-major-axis versus planet-mass plane. The colour-scale traces the initial formation region of the planetary seeds. Planet TOI-5795 b and its 3σ uncertainty range are shown in cyan.

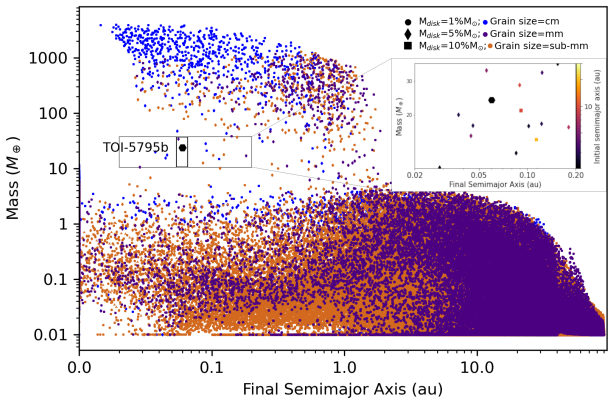

Fig. 10. Synthetic populations of 7.9×10^5 exoplanets generated sampling different initial circumstellar disc configurations (disc mass: 1, 5, 10% of the stellar mass; R_0: 40 and 90 au; pebble size: cm, mm, and sub-mm). Planet TOI-5795 b and its 3 σ uncertainty range are shown in black. The grey box indicates the range inwards of 0.2 au and the 3σ mass uncertainty range of the planet. The inset plot is a zoom-in of this window and shows, as a colour bar, the initial semi-major axis of the seeds.

masses of 1%, 5%, and 10% of the stellar mass, and characteristic radii R_0=40 au (compact disc) and R_0=90 au (extended disc). Although the resulting planetary populations contain more objects in the mass range of TOI-5795 b, once again only one synthetic planet falls within 3 σ of the real one (see Figure 10).

Finally, we explored the possibility that the migration prescription adopted in `GroMiT` does not provide an accurate description of the dynamical history of TOI-5795 b due to the uncertainty in migration efficiency (e.g. Pirani et al. 2019). Specifically, we focused on all synthetic planets with a final semi-major axis within 0.2 au. We found 14 synthetic planets that fit TOI-5795 b under this relaxed fitting criterion (see the zoom-in window in Figure 10), translating into a comparatively higher success rate, which, however, remains quite low in absolute terms (0.0018%). These best-fitting solutions arise from discs populated by pebbles that were either cm-sized or sub-mm sized, and with an initial mass of either 5% or 10% of the stellar mass of the system. The larger pebble size favours starting conditions beyond the water snowline while the smaller size favours initial conditions closer to the host star, suggesting differences in the bulk composition of the core (ice-rich versus rock-dominated).

Our results suggest that pebble accretion was not the dominant mechanism in forming this planet, or that it acted in combination with planetesimal accretion. This finding aligns with the conclusions of previous studies on exoplanets with similar masses (see Mantovan et al. 2024a; Naponiello et al. 2025a; Zingales et al. 2025), and with the challenges faced by population synthesis codes in capturing the full diversity of exoplanets. In their recent review, Burn & Mordasini (2025) compared several planet formation population synthesis codes, including some based on the pebble formation theory, and found that no model is currently capable of fully reproducing the observed mass-distance diagram of known planets, both among exoplanets and in the Solar System.

Given the mature age of the star, we also cannot exclude the possibility that this is not the planet as originally formed. Specifically, the present TOI-5795 b could be the product of a stochastic event, such as a merger between two or more smaller primordial planets in a system originally characterised by higher multiplicity (Turrini et al. 2020), as its modal eccentricity could be compatible with collisional damping after dynamical instability (Chambers 2001; Laskar & Petit 2017). Another explanation is that this planet may have formed at a larger orbital distance and been scattered inwards later, with its orbit becoming circularised after initially being eccentric. Given the still-large uncertainty in the eccentricity of the planet, exploring such a scenario is beyond the scope of this paper. Regardless, such an event would confuse, or even erase, the original formation path of this planet.

6. Atmospheric evaporation of TOI-5795 b

We investigated the evolutionary history of the atmosphere of TOI-5795 b since a close-in planet can be stripped of part of its atmosphere due to UV radiation from its parent star. Such an analysis is useful for evaluating how much atmosphere such a super-Neptune planet could have retained after evolution over several millions of years.

First, we selected a MESA evolutionary track (Choi et al. 2016), which recovers the stellar position at its nominal age in the $L_{\rm bol}$ vs. $T_{\rm eff}$ diagram, where $L_{\rm bol}$ is the bolometric luminosity of the host star. To this end, we considered a grid of evolutionary tracks for stars with masses and metallicities equal to the nominal values for TOI-5795, or equal to $\pm1\sigma$ values in both parameters (nine tracks in total). Some of these tracks are shown in Fig. 11. We find that the three tracks with nominal [Fe/H] = −0.27 (in green) appear to be too 'cool' relative to the parent star. The same occurs for the tracks with $M_\star$ = 0.9 $M_\odot$ (nominal value, in blue). Ultimately, we preferred the track with $M_\star$ = 0.846 $M_\odot$ (-1σ) and [Fe/H] = −0.20 ($+1\sigma$) (in orange), which provides the best match to the star's position in the luminosity–temperature diagram at its nominal age. This track was adopted in our modelling to determine the bolometric irradiation of the planet, and therefore its equilibrium temperature and core-envelope structure during evolution, accounting for gravitational shrinking (Fortney et al. 2007).

To model the evolution of high-energy irradiation, we needed to determine an anchor point for the X-ray luminosity at the current age. Since there is no X-ray detection available for this old, low-activity star, we considered as proxies the measured chromospheric $R'_{\rm HK}$ = −5.07 ± 0.02 index and the stellar age. Using the relationships from Mamajek & Hillenbrand (2008), the chromospheric index yields an X-ray luminosity $L_{\rm X} \sim 7\times10^{26}$ erg/s,

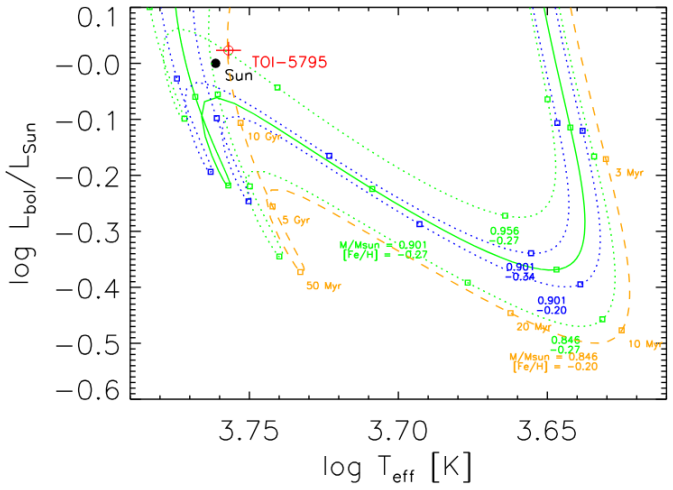

Fig. 11. Evolutionary track of TOI-5795 in the effective temperature-bolometric-luminosity plane. The red dot marks the current location of the star on the track.

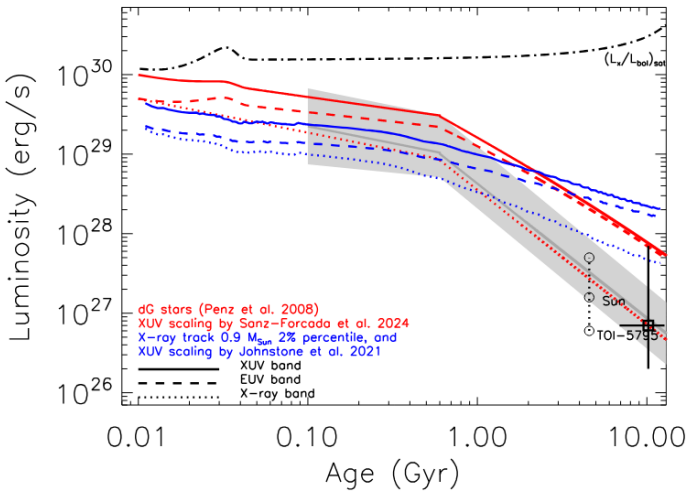

Fig. 12. Time evolution of X-ray (5–100 Å), EUV (100–920 Å), and total XUV luminosity of TOI-5795, according to Penz et al. (2008) and the X-ray/EUV scaling by Sanz-Forcada et al. (2025) (red lines) and according to Johnstone et al. (2021) (blue lines). Uncertainties on the age and X-ray luminosity of TOI-5795 are also indicated. The gray area shows the original locus for dG stars from Penz et al. (2008).

compatible with an age of approximately 8 Gyr. Assuming a rotational velocity of 2 km s^{-1}, we computed a lower limit on the rotational period of ≈30 d, which indicates an upper limit $L_X < 7 \times 10^{27}$ erg s^{-1}, using the activity-rotation relationship of Pizzolato et al. (2003). We also determined an uncertainty range in L_X from the relationship between the X-ray to the bolometric luminosity ratio and the Rossby number proposed by Wright et al. (2018). Taking into account uncertainties in both the stellar mass and the rotational period, we determined a conservative lower limit of 2×10^{26} erg s^{-1} for the X-ray luminosity.

Figure 12 shows the time evolution of the X-ray (5–100 Å), extreme ultraviolet (EUV; 100–920 Å), and XUV (X+EUV) luminosities, according to the X-ray luminosity evolution model of Penz & Micela (2008) coupled with the X-ray to EUV scaling law of Sanz-Forcada et al. (2025), or alternatively adopting the prescription of Johnstone et al. (2021). In the former case, the current X-ray luminosity appears to be near the median for solar-mass stars at ages of approximately 10 Gyr, such as TOI-5795. Alternatively, we selected the evolutionary track corresponding to the lowest 2% percentile of the activity distribution appropriate for stars with 0.9 $M_\odot$. Nonetheless, the Johnstone et al. (2021) evolutionary path yields an X-ray luminosity about a factor of four higher than the nominal value determined above, but still within the large uncertainty range. Given the very old age of TOI-5795, its current activity-rotation state is also compatible with the evolution of a star that started with a much higher rotation rate and activity level. For this reason, we also explored the results of photoevaporation assuming the Johnstone et al. (2021) track corresponding to the highest 98% percentile of the activity distribution. Under this assumption, the high-energy irradiation of the planet is possibly overestimated at late ages (>1 Gyr).

For the analysis of the past evaporative history, we employed the numerical code presented in Locci et al. (2019) and subsequently used it for the study of single systems (e.g. Maggio et al. (2022)). In this study, we considered three distinct evolutionary tracks for stellar XUV luminosity, referred to as the low state (track corresponding to the lowest 2% percentile of the activity distribution), the high state (track corresponding to the highest 2% percentile), and the PMSF track (based on the X-ray luminosity evolution of Penz & Micela 2008, combined with the X-ray to EUV conversion from Sanz-Forcada et al. 2025). In Fig. 13 we show the evolution of the mass, radius, and mass loss rate for the three scenarios.

Assuming an Earth-like core composition, we first calculated the planet's internal structure, finding a core mass of approximately 16.5 $M_\oplus$ and a radius of around 2 $R_\oplus$, which implies an atmospheric fraction of approximately 30%. We then computed the backwards evolution of key planetary parameters, such as mass and radius.

The mass-loss rates were estimated using the ATES analytical approximation (Caldiroli et al. 2021). At present, we find mass-loss rates of approximately 1.4×10^{10} g s^{-1} for the PMSF track, 2.6×10^{10} g s^{-1} for the low state, and 3×10^{10} g s^{-1} for the high state.

We followed the evolution back to an age of 10 million years, which we assumed to be the time when the accretion disc was fully dissipated and the planet had reached its final orbit. The inferred initial masses were approximately 30 $M_\oplus$ for the PMSF track, 28 $M_\oplus$ for the low state, and 33 $M_\oplus$ for the high state. The current mass of the planet is about 24 $M_\oplus$, indicating a mass loss of 9 $M_\oplus$ in the high state scenario, 6 $M_\oplus$ in the PMSF track, and 4 $M_\oplus$ in the low state.

We also observed a significant contraction of the planetary radius in all three cases. The predicted initial radii were approximately 11.2 $R_\oplus$ for the high state, 10.8 $R_\oplus$ for the PMSF track, and 10.5 $R_\oplus$ for the low state. The current planetary radius is around 6 $R_\oplus$, suggesting a large contraction mostly driven by gravitational compression, and possibly also by atmospheric loss.

7. Summary and discussion

Thanks to the continued discovery of candidate planets by the Transiting Exoplanet Survey Satellite (TESS) (Ricker et al. 2015) and the effort of follow-up groups, several planets have been found deep within the Neptune desert, as well as at its boundaries, over the past few years. These surprising discoveries include both low-density gaseous planets and high-density

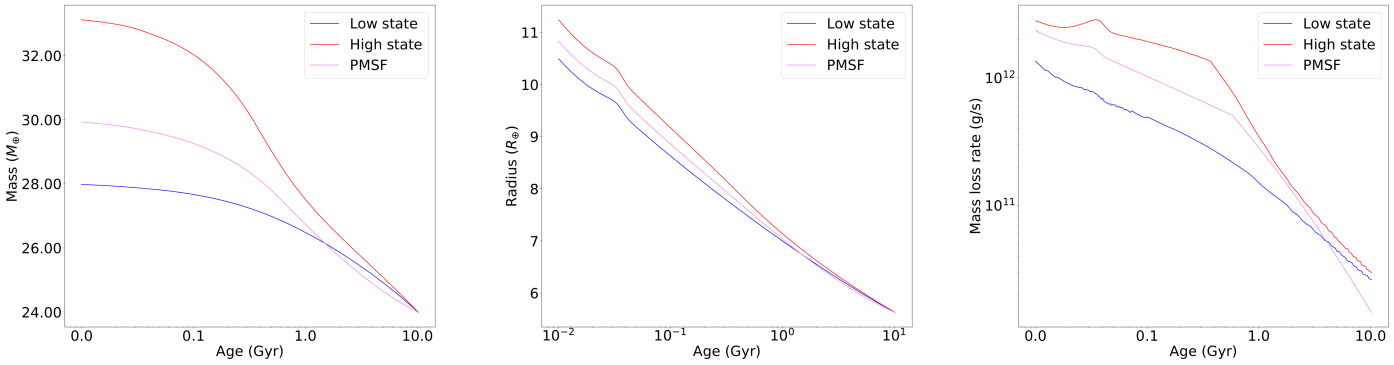

Fig. 13. Temporal evolution of mass, radius, and mass-loss rate of TOI-5795 b. The left, middle and right panels show the evolution of planetary mass, radius, and mass-loss rate, respectively. Colours indicate different high-energy evolutionary tracks: the blue line refers to the low state (lowest 2% percentile of the activity distribution), the red line refers to the high state (2% percentile), and the pink line refers to PMSF (based on the X-ray luminosity evolution of Penz & Micela 2008, combined with the X-ray to EUV conversion from Sanz-Forcada et al. 2025).

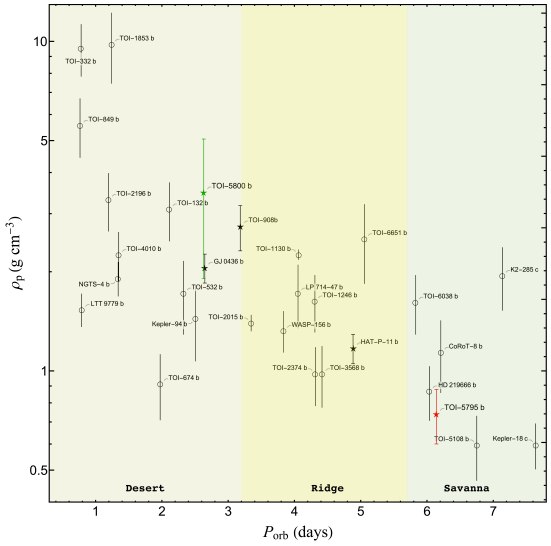

Fig. 14. Log-linear $\rho_p - P_{orb}$ diagram of known close-in transiting exoplanets with $3\,R_\oplus < R_p < 7\,R_\oplus$ and mean density measured with an accuracy to within 30%. Circles indicate the position of planets with eccentricity $e \leq 0.1$, while five-pointed stars indicate those with $e > 0.1$. The values of the parameters were taken from TEPCat. Horizontal error bars have been suppressed for clarity. Vertical error bars represent one standard deviation. The red star indicates the position of the new planet TOI-5795 b (see Sect. 4). The green star indicates the position of the new planet TOI-5800 b from our HONEI I paper (Naponiello et al. 2025b); its mean density has been measured with an accuracy <50%. The three coloured regions of the diagram are those recognised by Castro-González et al. (2024a).

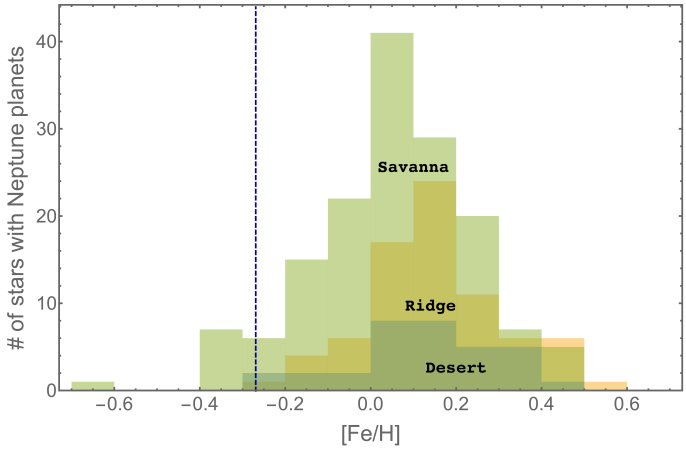

Fig. 15. Frequency distribution of parent-star metallicity for transiting exoplanets with $10\,M_\oplus < M_p < 100\,M_\oplus$ (Vissapragada & Behmard 2025). The histograms are shown with a 0.1 bin and for the three different populations identified by Castro-González et al. (2024a). 'Desert' refers to Neptune planets with orbital periods $P_{orb} < 3.2$ days; 'Ridge' to those with 3.2 days $< P_{orb} <$ 5.7 days; and 'Savanna' to those with 5.7 days $< P_{orb} <$ 100 days. Data were obtained on June 6, 2025 from TEPCat. The dashed vertical line marks the metallicity measured for the parent star of TOI-5795 b.

Neptunes, which are expected to be composed of a remarkable fraction of rocks (see Fig. 14[7]). The mean densities, ρ_p, of the known Neptune-size planets range from those of HATS-38 b (0.40 ± 0.07 g cm^{-3}; Espinoza-Retamal et al. 2024) and TIC 365102760 b (0.44 ± 0.15 g cm^{-3}; Grunblatt et al. 2024) to the extreme values of TOI-332 b (9.60 ± 1.10 g cm^{-3}; Osborn et al. 2023) and TOI-1853 b (9.74 ± 0.76 g cm^{-3}; Naponiello et al. 2023). This diversity challenges conventional theories of planetary formation and evolution and calls for other hypotheses, such as catastrophic formation scenarios (e.g. multiple planetary collisions; Naponiello et al. 2023).

We have confirmed and characterised TOI-5795 b, a new super-Neptune planet ($M_p = 23.66^{+4.09}_{-4.60}\,M_\oplus$; $R_p = 5.62 \pm 0.11\,R_\oplus$) orbiting a metal-poor G3 V star on a 6.14-day orbit, consistent with being circular. Its position in the mass-period plane lies at the border between the ridge and the savanna (see Fig. 8).

Very recently, Vissapragada & Behmard (2025) presented a demographic study, based on data from *Gaia* DR3 (Gaia Collaboration 2023), considering the metallicities of stars hosting Neptune-sized planets. They report that planets in the Neptune desert and ridge orbit stars significantly more metal-rich than hosts of smaller planets. The 'top-down' theory, which proposes that Neptune desert planets are the exposed interiors of former gas giants, predicts that their host stars should be metal-rich, similar to hot Jupiters. The host-star population of Neptune-savanna planets was found to be significantly less metal-rich. The metal-poor nature of TOI-5795 ([Fe/H] = −0.27 ± 0.07) aligns with the characteristics expected for Neptune-savanna

[7] Data taken from the Transiting Extrasolar Planet Catalog (TEPCat), available at https://www.astro.keele.ac.uk/jkt/tepcat/ (Southworth 2011) as of June 2025.

hosts, contrasting sharply with the metal-rich hosts typically found for Neptune-desert planets (Castro-González et al. 2024b), see Fig. 15. Another property of savanna planets is that they are typically low density compared to the higher-density ridge and desert planets (Castro-González et al. 2024b), and 5795 b also fits this paradigm (see Fig. 14).

The characteristics of the TOI-5795 planetary system support the view that planets in the savanna are unlikely to have formed through the top-down mechanism and probably have a distinct origin and evolution history compared to the hottest Neptunes in the desert. In this context, we conducted further investigation by simulating numerous planetary formation scenarios within a protoplanetary disc, varying factors such as initial position, seed input time, and disc viscosity (see Sect. 5). Despite extensive simulations, few simulated planets accurately matched the observed characteristics of TOI-5795 b, indicating challenges in explaining its formation through current pebble accretion theory. This discrepancy might be due to uncertainties in migration prescriptions within the code or the inherent difficulty in forming planets of TOI-5795 b's mass via pebble accretion, also acknowledging the possibility of stochastic events such as three-body interactions or mergers.

By determining the time evolution of the parent star's high-energy irradiation, we also investigated the impact of UV radiation from the parent star in stripping part of the planet's atmosphere over billions of years. Since TOI-5795 is very old ($10.2^{+2.5}_{-3.3}$ Gyr), its initial rotation period is poorly constrained. Therefore, we considered three different evolutionary tracks for XUV radiation, which produce significantly different results, as discussed in Sect. 6. The evolution was tracked back to an age of 10 million years, which is assumed to be when the accretion disc dissipated and the planet reached its final orbit. We estimated that TOI-5795 b may have lost a significant portion (14% − 27%) of its initial mass due to atmospheric evaporation. In the high-state scenario, the planet experienced the largest mass loss, estimated at $9\,M_\oplus$ from an initial mass of approximately $33\,M_\oplus$. This scenario may overestimate high-energy irradiation at late ages. Under the PMSF track, the planet lost $6\,M_\oplus$ from an initial mass of approximately $30\,M_\oplus$. In the low-state scenario, the planet lost $4\,M_\oplus$ from an initial mass of approximately $28\,M_\oplus$. Owing to its large mass, TOI-5795 retains a large part of its atmosphere, ending its evolution with about 32% of its mass in the atmosphere. Along with mass loss, a significant contraction in the planetary radius was observed across all three scenarios. The predicted initial radii were approximately $11.2\,R_\oplus$ (high state), $10.8\,R_\oplus$ (PMSF track), and $10.5\,R_\oplus$ (low state). The current planetary radius is around $6\,R_\oplus$, indicating a strong contraction driven primarily by gravitational compression.

Using the parameters of the star (Table 1) and the planet (Table 2), we estimated the transmission spectroscopy metric (TSM; Kempton et al. 2018) of TOI-5795 b, which, considering its equilibrium temperature ($T_{\rm eq}$ = 1136 ± 18 K.), is relatively high at 103^{+25}_{-15}. This makes TOI-5795 b a promising candidate for possible atmospheric characterisation with space telescopes. Notably, TOI 5795.01 is included in a list of TESS candidates that are potentially suitable for Ariel observations.[8] The present confirmation of TOI 5795.01 as a planet is, therefore, valuable for the ongoing preparatory science work of the Ariel Science Consortium (Tinetti et al. 2022).

Acknowledgements. This work is based on observations collected at the European Organization for Astronomical Research in the Southern Hemisphere under ESO programme 113.26UJ.001. This work includes data collected with the TESS mission, obtained from the MAST data archive at the Space Telescope Science Institute (STScI). Funding for the TESS mission is provided by the NASA Explorer Program. STScI is operated by the Association of Universities for Research in Astronomy, Inc., under the NASA contract NAS 5–26555. The authors acknowledge the use of public TESS data from pipelines at the TESS Science Office and at the TESS Science Processing Operations Center. Resources supporting this work were provided by the NASA High-End Computing (HEC) Program through the NASA Advanced Supercomputing (NAS) Division at Ames Research Center for the production of the SPOC data products. This research has used the Exoplanet Follow-up Observation Program (ExoFOP; DOI: 10.26134/ExoFOP5) website, which is operated by the California Institute of Technology, under contract with the National Aeronautics and Space Administration under the Exoplanet Exploration Program. This research has used the NASA Exoplanet Archive, which is operated by the California Institute of Technology, under contract with the National Aeronautics and Space Administration under the Exoplanet Exploration Program. This work makes use of observations from the LCOGT network. Part of the LCOGT telescope time was granted by NOIRLab through the Mid-Scale Innovation Program (MSIP). MSIP is funded by NSF. L.M. acknowledges the financial contribution from the PRIN MUR 2022 project 2022J4H55R. KAC and CNW acknowledge support from the TESS mission via subaward s3449 from MIT. L.N. acknowledges financial contribution from the INAF Large Grant 2023 "EXODEMO". This work has made use of data from the European Space Agency (ESA) mission *Gaia* (https://www.cosmos.esa.int/gaia), processed by the *Gaia* Data Processing and Analysis Consortium (DPAC, https://www.cosmos.esa.int/web/gaia/dpac/consortium). Funding for the DPAC has been provided by national institutions, in particular the institutions participating in the *Gaia* Multilateral Agreement. MP acknowledges financial support from the European Union – NextGenerationEU (PRIN MUR 2022 20229R43BH) and the "Programma di Ricerca Fondamentale INAF 2023". The authors gratefully acknowledge the coordination of the HARPS time sharing, which was essential to this work.

[8] https://exofop.ipac.caltech.edu/tess/view_toi_ariel.php.

References

Adamow, M. M. 2017, in American Astronomical Society Meeting Abstracts, 230, 216.07
Akeson, R. L., Chen, X., Ciardi, D., et al. 2013, PASP, 125, 989
Aller, A., Lillo-Box, J., Jones, D., Miranda, L. F., & Barceló Forteza, S. 2020, A&A, 635, A128
Amarsi, A. M., Asplund, M., Collet, R., & Leenaarts, J. 2015, MNRAS, 454, L11
Andrews, S. M. 2020, ARA&A, 58, 483
Armitage, P. J. 2020, Astrophysics of planet formation (Cambridge: Cambridge University Press)
Astropy Collaboration (Price-Whelan, A. M., et al.) 2018, AJ, 156, 123
Baraffe, I., Homeier, D., Allard, F., & Chabrier, G. 2015, A&A, 577, A42
Biazzo, K., D'Orazi, V., Desidera, S., et al. 2022, A&A, 664, A161
Bitsch, B., Morbidelli, A., Johansen, A., et al. 2018, A&A, 612, A30
Bourrier, V., Lecavelier des Etangs, A., Ehrenreich, D., et al. 2018, A&A, 620, A147
Brown, T. M., Baliber, N., Bianco, F. B., et al. 2013, PASP, 125, 1031
Bryson, S. T., Jenkins, J. M., Klaus, T. C., et al. 2010, SPIE Conf. Ser., 7740, 77401D
Bryson, S. T., Jenkins, J. M., Klaus, T. C., et al. 2020, Kepler Data Processing Handbook: Target and Aperture Definitions: Selecting Pixels for Kepler Downlink, Kepler Science Document KSCI-19081-003, id. 3, ed. J. M. Jenkins.
Burn, R., & Mordasini, C. 2025, Planetary Population Synthesis, eds. H. J. Deeg, & J. A. Belmonte (Cham: Springer Nature Switzerland), 1
Caldiroli, A., Haardt, F., Gallo, E., et al. 2021, A&A, 655, A30
Castelli, F. & Kurucz, R. L. 2003, in Modelling of Stellar Atmospheres, 210, eds. N. Piskunov, W. W. Weiss, & D. F. Gray, A20
Castro-González, A., Bourrier, V., Lillo-Box, J., et al. 2024a, A&A, 689, A250
Castro-González, A., Lillo-Box, J., Armstrong, D. J., et al. 2024b, A&A, 691, A233
Chambers, J. E. 2001, Icarus, 152, 205
Choi, J., Dotter, A., Conroy, C., et al. 2016, ApJ, 823, 102
Ciardi, D. R., Beichman, C. A., Horch, E. P., & Howell, S. B. 2015, ApJ, 805, 16
Collins, K. A., Kielkopf, J. F., Stassun, K. G., & Hessman, F. V. 2017, AJ, 153, 77
Cutri, R. M., Wright, E. L., Conrow, T., et al. 2021, VizieR Online Data Catalog: AllWISE Data Release (Cutri+ 2013), VizieR On-line Data Catalog: II/328. Originally published in: IPAC/Caltech (2013)
Dekany, R., Roberts, J., Burruss, R., et al. 2013, ApJ, 776, 130

Doyle, A. P., Davies, G. R., Smalley, B., Chaplin, W. J., & Elsworth, Y. 2014, MNRAS, 444, 3592
Eastman, J., Gaudi, B. S., & Agol, E. 2013, PASP, 125, 83
Eastman, J. 2017, EXOFASTv2: Generalized publication-quality exoplanet modeling code, Astrophysics Source Code Library [record ascl:1710.003]
Eastman, J. D., Rodriguez, J. E., Agol, E., et al. 2019, arXiv e-prints [arXiv:1907.09480]
Ehrenreich, D., Bourrier, V., Wheatley, P. J., et al. 2015, Nature, 522, 459
Espinoza, N. 2018, RNAAS, 2, 209
Espinoza, N., Kossakowski, D., & Brahm, R. 2019, MNRAS, 490, 2262
Espinoza-Retamal, J. I., Stefánsson, G., Petrovich, C., et al. 2024, AJ, 168, 185
Esposito, M., Covino, E., Mancini, L., et al. 2014, A&A, 564, L13
Foreman-Mackey, D., Agol, E., Ambikasaran, S., & Angus, R. 2017, AJ, 154, 220
Fortney, J. J., Marley, M. S., & Barnes, J. W. 2007, ApJ, 659, 1661
Fulton, B. J., Petigura, E. A., Blunt, S., & Sinukoff, E. 2018, PASP, 130, 044504
Furlan, E., Ciardi, D. R., Everett, M. E., et al. 2017, AJ, 153, 71
Gaia Collaboration (Vallenari, A., et al.) 2023, A&A, 674, A1
Gomes da Silva, J., Figueira, P., Santos, N., & Faria, J. 2018, J. Open Source Softw., 3, 667
Grunblatt, S. K., Saunders, N., Huber, D., et al. 2024, AJ, 168, 1
Guerrero, N. M., Seager, S., Huang, C. X., et al. 2021, ApJS, 254, 39
Hawthorn, F., Bayliss, D., Wilson, T. G., et al. 2023, MNRAS, 520, 3649
Hayward, T. L., Brandl, B., Pirger, B., et al. 2001, PASP, 113, 105
Henden, A. A., Templeton, M., Terrell, D., et al. 2016, VizieR Online Data Catalog: AAVSO Photometric All Sky Survey (APASS) DR9 (Henden+, 2016), VizieR On-line Data Catalog: II/336. Originally published in: 2015AAS...22533616H
Høg, E., Fabricius, C., Makarov, V. V., et al. 2000, A&A, 355, L27
Ida, S., Guillot, T., & Morbidelli, A. 2016, A&A, 591, A72
Ionov, D. E., Pavlyuchenkov, Y. N., & Shematovich, V. I. 2018, MNRAS, 476, 5639
Jenkins, J. M., Twicken, J. D., McCauliff, S., et al. 2016, SPIE Conf. Ser., 9913, 99133E
Johansen, A., Ida, S., & Brasser, R. 2019, A&A, 622, A202
Johnstone, C. P., Bartel, M., & Güdel, M. 2021, A&A, 649, A96
Kempton, E. M. R., Bean, J. L., Louie, D. R., et al. 2018, PASP, 130, 114401
Kipping, D. M. 2013, MNRAS, 435, 2152
Koskinen, T. T., Lavvas, P., Huang, C., et al. 2022, ApJ, 929, 52
Kreidberg, L. 2015, PASP, 127, 1161
Kunimoto, M., Vanderburg, A., Huang, C. X., et al. 2023, AJ, 166, 7
Laskar, J., & Petit, A. C. 2017, A&A, 605, A72
Lightkurve Collaboration (Cardoso, J. V. d. M., et al.) 2018, Lightkurve: Kepler and TESS time series analysis in Python, Astrophysics Source Code Library [record ascl:1812.013]
Locci, D., Cecchi-Pestellini, C., & Micela, G. 2019, A&A, 624, A101
Maggio, A., Locci, D., Pillitteri, I., et al. 2022, ApJ, 925, 172
Mamajek, E. E., & Hillenbrand, L. A. 2008, ApJ, 687, 1264
Mantovan, G., Malavolta, L., Locci, D., et al. 2024a, A&A, 684, L17
Mantovan, G., Wilson, T. G., Borsato, L., et al. 2024b, A&A, 691, A67
Matsakos, T., & Königl, A. 2016, ApJ, 820, L8
Mayor, M., Pepe, F., Queloz, D., et al. 2003, The Messenger, 114, 20
Mazeh, T., Holczer, T., & Faigler, S. 2016, A&A, 589, A75
McCully, C., Volgenau, N. H., Harbeck, D.-R., et al. 2018, SPIE Conf. Ser., Vol 10707, 107070K
Naponiello, L., Mancini, L., Damasso, M., et al. 2022, A&A, 667, A8
Naponiello, L., Mancini, L., Sozzetti, A., et al. 2023, Nature, 622, 255
Naponiello, L., Bonomo, A. S., Mancini, L., et al. 2025a, A&A, 693, A7
Naponiello, L., Vissapragada, S., Bonomo, A. S., et al. 2025b, A&A, 701, A79
Osborn, A., Armstrong, D. J., Fernández Fernández, J., et al. 2023, MNRAS, 526, 548
Owen, J. E., & Jackson, A. P. 2012, MNRAS, 425, 2931
Owen, J. E., & Lai, D. 2018, MNRAS, 479, 5012
Paxton, B., Marchant, P., Schwab, J., et al. 2015, ApJS, 220, 15
Pecaut, M. J., & Mamajek, E. E. 2013, ApJS, 208, 9
Penz, T., & Micela, G. 2008, A&A, 479, 579
Penz, T., Micela, G., & Lammer, H. 2008, A&A, 477, 309
Pepe, F., Mayor, M., Rupprecht, G., et al. 2002, The Messenger, 110, 9
Pepe, F., Ehrenreich, D., & Meyer, M. R. 2014, Nature, 513, 358
Pirani, S., Johansen, A., Bitsch, B., Mustill, A. J., & Turrini, D. 2019, A&A, 623, A169
Pizzolato, N., Maggio, A., Micela, G., Sciortino, S., & Ventura, P. 2003, A&A, 397, 147
Polychroni, D., Turrini, D., & Pirani, S. 2023, https://doi.org/10.5281/zenodo.10593198
Ricker, G. R., Winn, J. N., Vanderspek, R., et al. 2015, J. Astron. Telesc. Instrum. Syst., 1, 014003
Rosotti, G. P. 2023, New A Rev., 96, 101674
Sanz-Forcada, J., López-Puertas, M., Lampón, M., et al. 2025, A&A, 693, A285
Skrutskie, M. F., Cutri, R. M., Stiening, R., et al. 2006, AJ, 131, 1163
Smith, J. C., Stumpe, M. C., Van Cleve, J. E., et al. 2012, PASP, 124, 1000
Sneden, C. 1973, ApJ, 184, 839
Sousa, S. G., Santos, N. C., Adibekyan, V., Delgado-Mena, E., & Israelian, G. 2015, A&A, 577, A67
Southworth, J. 2011, MNRAS, 417, 2166
Speagle, J. S. 2020, MNRAS, 493, 3132
Stumpe, M. C., Smith, J. C., Van Cleve, J. E., et al. 2012, PASP, 124, 985
Stumpe, M. C., Smith, J. C., Catanzarite, J. H., et al. 2014, PASP, 126, 100
Stassun, K. G., Oelkers, R. J., Pepper, J., et al. 2018, AJ, 156, 102
Stassun, K. G., Oelkers, R. J., Paegert, M., et al. 2019, AJ, 158, 138
Szabó, G. M., Kálmán, S., Borsato, L., et al. 2023, A&A, 671, A132
Szentgyorgyi, A. H., & Furész, G. 2007, in Revista Mexicana de Astronomia y Astrofisica Conference Series, 28, ed. S. Kurtz, 129
Tanaka, H., Murase, K., & Tanigawa, T. 2020, ApJ, 891, 143
Testi, L., Natta, A., Manara, C. F., et al. 2022, A&A, 663, A98
Thompson, S. E., Coughlin, J. L., Hoffman, K., et al. 2018, ApJS, 235, 38
Thorngren, D. P., Lee, E. J., & Lopez, E. D. 2023, ApJ, 945, L36
Tinetti, G., Eccleston, P., Lueftinger, T., et al. 2022, in European Planetary Science Congress, EPSC2022-1114
Tokovinin, A., Mason, B. D., Hartkopf, W. I., Mendez, R. A., & Horch, E. P. 2018, AJ, 155, 235
Turrini, D., Zinzi, A., & Belinchon, J. A. 2020, A&A, 636, A53
Turrini, D., Marzari, F., Polychroni, D., et al. 2023, A&A, 679, A55
Twicken, J. D., Clarke, B. D., Bryson, S. T., et al. 2010, in Software and Cyberinfrastructure for Astronomy, 7740, eds. N. M. Radziwill, & A. Bridger, International Society for Optics and Photonics (SPIE), 749
Vissapragada, S., & Behmard, A. 2025, AJ, 169, 117
Wilson, T. G., Goffo, E., Alibert, Y., et al. 2022, MNRAS, 511, 1043
Wright, N. J., Newton, E. R., Williams, P. K. G., Drake, J. J., & Yadav, R. K. 2018, MNRAS, 479, 2351
Zechmeister, M., & Kürster, M. 2009, A&A, 496, 577
Zechmeister, M., Reiners, A., Amado, P. J., et al. 2018, A&A, 609, A12
Ziegler, C., Tokovinin, A., Briceño, C., et al. 2020, AJ, 159, 19
Zingales, T., Malavolta, L., Borsato, L., et al. 2025, A&A, 695, A273

Appendix A: Additional figures and tables

Table A.1. TRES and HARPS radial-velocities and relative errors of TOI-5795.

BJD_{TDB} [days]	RV [m s^{-1}]	σ_{RV} [m s^{-1}]	$\sigma_{RV\ with\ jtter}$ [m s^{-1}]
HARPS			
2460490.8329	−9.20	1.98	4.24
2460492.6482	−6.26	2.27	4.39
2460493.7177	9.37	2.23	4.36
2460495.7240	−13.45	4.29	5.69
2460497.7079	−8.41	2.29	4.39
2460498.6601	−1.96	1.96	4.23
2460499.7998	3.12	2.09	4.29
2460500.7406	5.94	2.30	4.39
2460503.6988	−0.26	3.66	5.24
2460504.6547	−11.44	2.73	4.64
2460516.6357	−10.17	3.87	5.39
2460517.7241	2.39	2.48	4.49
2460519.7068	−3.49	2.91	4.75
2460530.6715	10.72	3.00	4.80
2460531.6555	−2.31	3.84	5.37
2460532.6626	−10.49	2.63	4.58
2460533.5801	−5.16	2.89	4.73
2460534.6866	−10.83	2.19	4.34
2460535.6932	1.77	1.70	4.12
TRES			
2459864.5963	−59	30	
2459879.6927	−31	21	
2460269.6029	−23	31	
2460271.5714	21	30	
2460272.5841	45	25	
2460281.5673	81	28	
2460282.5692	−23	15	
2460296.5677	61	27	
2460554.8071	69	33	
2460562.7231	63	33	
2460577.6931	−7	24	
2460608.5804	−56	19	

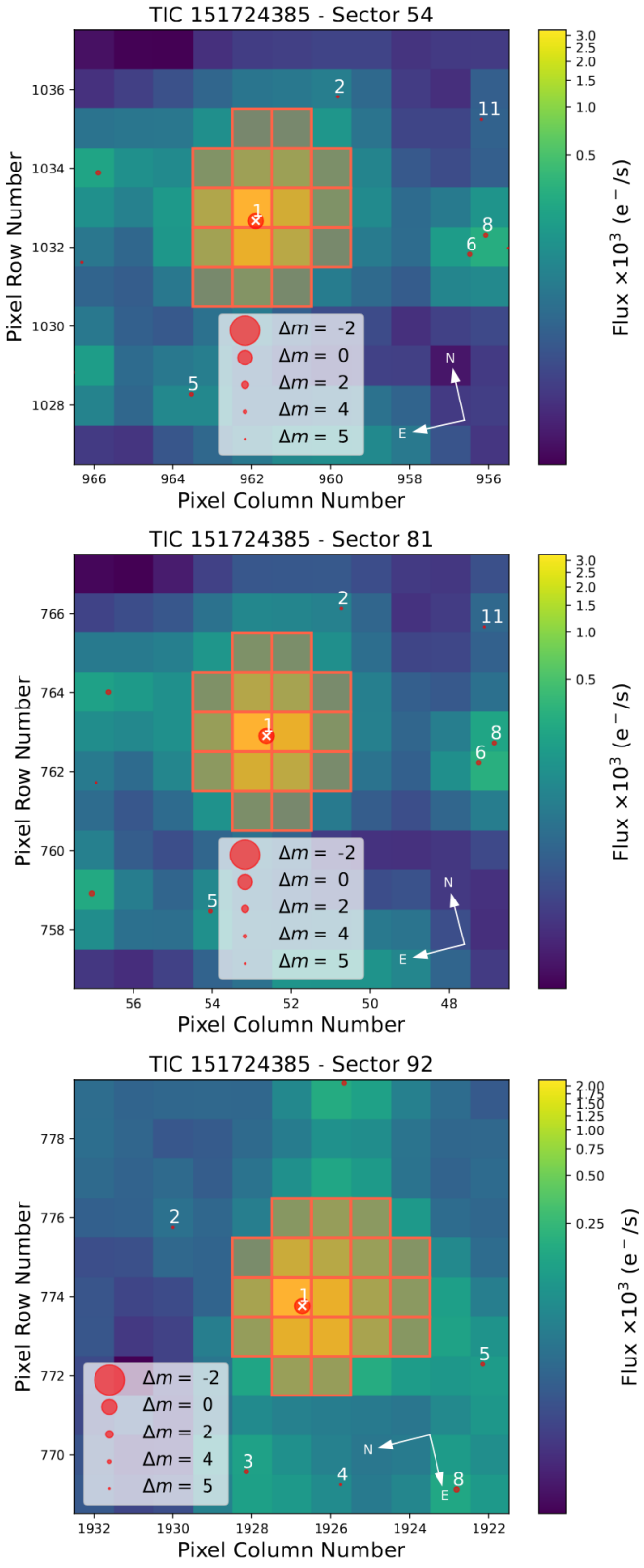

Fig. A.1. Target pixel files from the TESS observation of Sector 54 (top panel), Sector 81 (middle panel), and Sector 92 (bottom panel). TOI-5795 is indicated by a white cross. The SPOC pipeline aperture is shown by shaded red squares. Gaia DR3 catalogue (Gaia Collaboration 2023) is overlaid with symbol sizes proportional to the magnitude difference with TOI-5795.

Appendix B: Detection sensitivity

We estimated the completeness of both the TRES and HARPS RV time series by performing injection-recovery simulations, in which RVs with synthetic planetary signals were injected at the times of our observations. The details of the simulation can be found in Naponiello et al. 2025a and the results are shown in Fig. B.1. Thanks to the HARPS dataset, we are sensitive to planets up to roughly the mass of Jupiter placed at 1 au, though their signals would only appear as linear and quadratic trends, while TRES is slightly more sensitive to distant, very massive ($\sim$10 $M_{\rm jup}$) planets, despite a lower resolution, owing to its longer timeline.

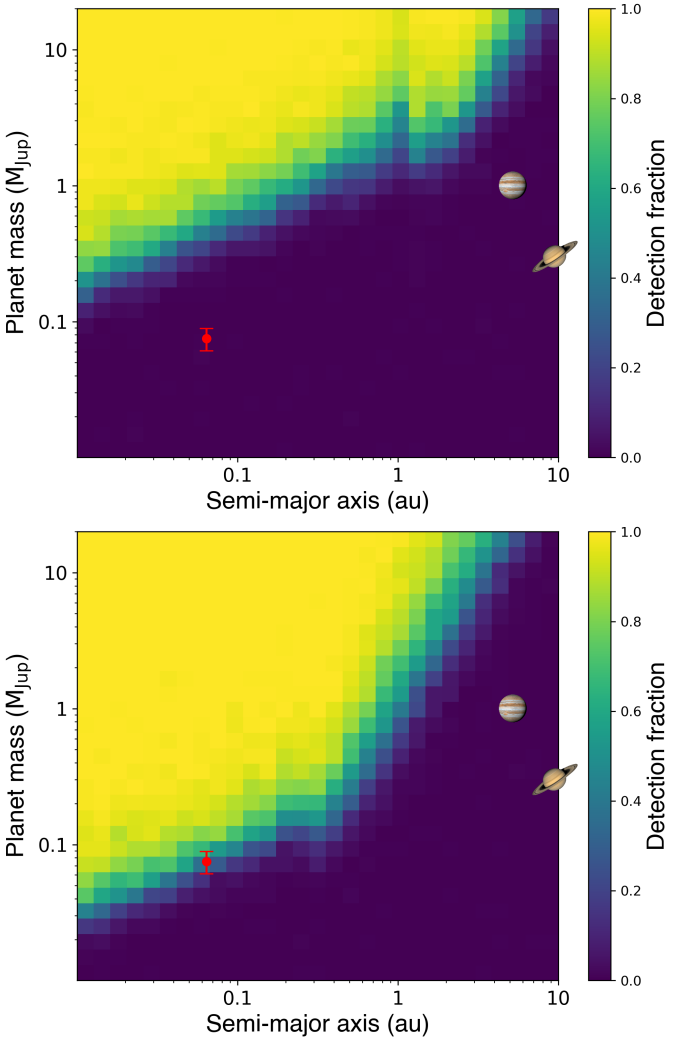

Fig. B.1. TRES (top panel) and HARPS (bottom panel) RV detection maps for TOI-5795. The color scale expresses the detection fraction, while the red circle marks the position of TOI-5795 b. Jupiter and Saturn are shown for comparison.